nature physics

Article

https://doi.org/10.1038/s41567-025-03129-8

Temporal anti-parity–time symmetry in diffusive transport

Received: 17 July 2025

Accepted: 4 November 2025

Published online: 10 December 2025

Check for updates

Peng Jin[1,2,3,6], Chengmeng Wang[2,6], Yuhong Zhou[2,6], Shuihua Yang[3,6], Fubao Yang[4], Jinrong Liu[1], Ya Sun[3,5], Pengfei Zhuang[2], Yiyang Zhang[2], Liujun Xu[4], Yi Zhou[3], Ghim Wei Ho[3], Cheng-Wei Qiu[3] ✉ & Jiping Huang[2] ✉

Parity–time symmetry has revolutionized wave and energy transport control in non-Hermitian systems, yet has so far been mostly explored in static phases, where a system's behaviour is locked into a fixed-symmetric or broken-symmetry phase. The vast potential of time-domain dynamics has remained largely untapped. Here we introduce the concept of temporal anti-parity–time symmetry, a principle that allows the transport dynamics of a system to be actively shaped in real time. Rather than designing static phases, we influence the timing of non-Hermitian phase transitions, making the system's temporal evolution itself a programmable degree of freedom. Through the dynamic control of material properties and convective flow, we dictate the exact moments these transitions occur, thereby controlling the entire transport history of the system. This temporal control achieves highly tunable field localization and realizes counterintuitive thermal transport, enabling temperature profiles to move forwards with convection, backwards against it or remain trapped at arbitrary locations. Our findings extend non-Hermitian physics into the time domain and establish a framework for on-demand wave and energy transport.

Physical symmetries dictate the fundamental rules of interaction and evolution in nature[1]. The advent of parity–time (PT) symmetry launched a paradigm shift in non-Hermitian physics, demonstrating that open systems with balanced gain and loss can counterintuitively possess entirely real energy spectra[2,3]. At the heart of this revolution are exceptional points (EPs): unique degeneracies at which a system's eigenvalues and eigenvectors simultaneously coalesce[4,5]. Harnessing these EPs has provided an unprecedented platform for sculpting the flow of energy and information[6]. Landmark demonstrations, including ultrasensitive sensors[7] and robust single-mode lasers[8,9], have showcased their power. Moreover, EPs have enabled deep probes into fundamental phenomena like phonon laser dynamics[10] and enhanced nonlinearities[11], firmly establishing the non-Hermitian toolkit across diverse fields from photonics[12–14] to acoustics[15,16] and magnonics[17]. Anti-parity–time (APT) symmetry, which maps a Hamiltonian to its negative, further expands this landscape, promising new ways to command energy transport[18–21].

Non-Hermitian physics has recently been generalized to diffusive systems, enabling remarkable static phenomena such as heat localization[22,23] and topological thermal states[24–29]. These advances, however, have been confined to a static paradigm in which systems with time-invariant properties are designed merely to characterize their fixed-symmetric or broken-symmetry phases[28–30]. Such approaches

[1]College of Science, University of Shanghai for Science and Technology, Shanghai, China. [2]Department of Physics, State Key Laboratory of Surface Physics, and Key Laboratory of Micro and Nano Photonic Structures (Ministry of Education), Fudan University, Shanghai, China. [3]Department of Electrical and Computer Engineering, National University of Singapore, Singapore, Singapore. [4]Graduate School of China Academy of Engineering Physics, Beijing, China. [5]State Key Laboratory of Metal Matrix Composites, School of Materials Science and Engineering, Shanghai Jiao Tong University, Shanghai, China. [6]These authors contributed equally: Peng Jin, Chengmeng Wang, Yuhong Zhou, Shuihua Yang. ✉e-mail: chengwei.qiu@nus.edu.sg; jphuang@fudan.edu.cn

https://doi.org/10.1038/s41567-025-03129-8

inherently lack the capacity to dynamically manipulate energy transport—such as actively dragging or trapping heat—due to a fundamental technical barrier: the challenge of precisely modulating lattice couplings in time to drive temporally controlled phase transitions. This requires the rapid, on-demand tuning of heat exchange pathways within the medium, a capability yet to be realized experimentally. Diffusive systems present a particularly promising avenue to address this challenge[31–37]. Unlike wave-based systems, whose temporal control is spatially restricted by intrinsic diffraction limits[38,39], diffusive transport is determined by structural properties[40–44] rather than characteristic wavelengths. This crucial difference provides the precise spatial localization needed to unlock an entirely new dimension of temporally modulated phenomena.

Here we unlock this missing dimension of temporal control by introducing the concept of temporal APT symmetry. Instead of characterizing effective static phases with periodic modulation[45–47], we treat the timing of non-Hermitian phase transitions themselves as a programmable degree of freedom, scripted through the dynamic modulation of both material properties and convective flow. The result is an unprecedented command over thermal energy: we demonstrate the ability to catch a thermal profile in transit, drive it forwards with convection, reverse it against the flow or trap it at any desired location. In a three-ring thermal system with a time-tailored lattice coupling, we establish and experimentally validate this new paradigm, developing a complete framework that seamlessly integrates theory and deep-learning-driven design with experimental proof. This work fundamentally moves non-Hermitian physics into the time domain and pioneers a new paradigm for intelligent, on-demand energy transport.

Temporal APT symmetry engineering

Traditional non-Hermitian systems, although powerful, remain constrained to static configurations. Here we introduce and realize a fundamentally different approach: a system in which temporal APT symmetry allows the entire transport history to be dynamically scripted. To achieve this, we designed a three-ring thermal metadevice (Fig. 1). The two counter-rotating outer rings introduce programmable convection, establishing a balanced gain–loss landscape essential for APT symmetry. The central ring, whose material properties can be altered on demand, acts as a time-tailored thermal coupling, providing the crucial degree of freedom to control the timing of the non-Hermitian phase transition, t_0.

This architecture enables a two-phase temporal protocol. In the initial 'transport phase', the system is configured to propel a thermal wave packet either forwards with convection or backwards against it. At a precisely determined moment t_0, the system executes a programmed switch into the 'trapping phase'. This is accomplished by simultaneously adjusting the material composition of the central ring and reconfiguring the rotational velocities of the outer rings. Specifically, ring 1 maintains its rotation, ring 2 stops rotating and transitions from an air-embedded to a copper-embedded structure, and ring 3 rotates at velocity $-v$. These concurrent changes shift the system into an APT-symmetric state, characterized by a heat exchange rate h exceeding the EP threshold ($h > h_{EP}$). This action effectively freezes the thermal wave packet at its target location. Here 'freezing' (or 'trapping') denotes the localization and phase locking of temperature modulation, not a standing wave without energy dissipation.

The system's dynamics are governed by a time-dependent complex eigenfrequency $\omega(t)$, engineered by switching the system's parameters at time t_0. The evolution of a thermal wave packet, $T \approx e^{i(kx-\omega t)}$ (where k denotes the wave number), is dictated by the real part of this eigenfrequency (Supplementary Sections 1 and 2), Re $[\omega(t)]$. Throughout, we use 'wave' and 'wave packet' to denote diffusive temperature modulations with complex frequency (pseudo-waves) arising from the convective–diffusive, non-Hermitian dynamics, rather than lossless

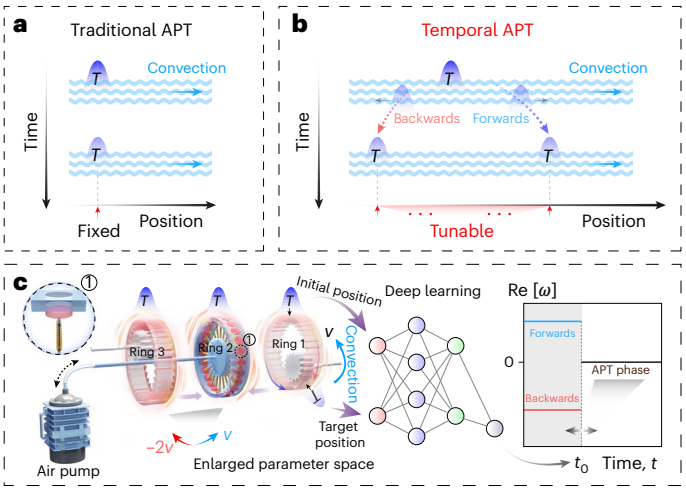

Fig. 1 | Engineering temporal APT symmetry. a, Traditional APT symmetry traps a thermal wave packet within a convective medium (waves; arrows indicate the flow direction) by suppressing convection intensity. As time progresses, the wave packet remains localized but gradually dissipates, shown as a fainter packet at the same position. **b**, Temporal APT symmetry, under identical convective conditions, allows the active trapping of heat at arbitrary locations. By implementing temporal modulation, heat transport (with accompanying dissipation) can occur either forwards (aligned with convection) or backwards (against convection), enabling tunable spatial control. **c**, Experimental setup. The system consists of three concentric rotating rings, each independently driven via motor-gear assemblies. Two outer copper rings exchange heat via an intermediate ring constructed from aluminium alloy 6061, which can incorporate either air or copper inserts via an air pump. All rings initially possess the same imposed temperature distribution, described by a wave packet of the form $T \approx e^{i(kx-\omega t)}$. Initially, ring 1 rotates at velocity v, whereas rings 2 and 3 rotate at v ($-2v$) for forward (backward) heat transport. At a specific temporal switching moment t_0, the middle ring's internal composition (air or copper inserts) as well as the angular velocities of rings 2 and 3 are abruptly modified (enlarged parameter space), thereby modulating the heat exchange rate h and creating a temporal APT-symmetric configuration. A deep learning model predicts the optimal switching time t_0 from the initial position θ_0, target position θ_T and system parameters, thereby enabling precise control over the temporal evolution of ring 1's eigenfrequency ω.

propagating waves. This temporal protocol is mathematically captured by

$$\mathrm{Re}\,[\omega(t)]\begin{cases} > 0\ (\text{forwards}),\ t \le t_0 \\ < 0\ (\text{backwards}),\ t \le t_0\,. \\ = 0\ (\text{trapping}),\ t > t_0 \end{cases} \tag{1}$$

This active, real-time engineering of the eigenfrequency spectrum is the fundamental mechanism for our temporal control.

Analytical methods struggle to accurately predict the temperature evolution in our system (Supplementary Sections 1 and 2). This difficulty arises primarily because the intermediate layer's thickness is comparable with the outer rings', strongly influencing the heat exchange dynamics in non-negligible ways. To circumvent this limitation, we developed a deep learning model to determine the optimal switching time t_0. For a detailed account of the physics captured by the artificial neural network (ANN) beyond the analytical methods, see Supplementary Section 3. The ANN maps the normalized initial (x_0^{Norm}) and target (x_T^{Norm}) peak positions to the required t_0 (Fig. 1c):

$$t_0 = f^{(N)}\left(W^{(N)} f^{(N-1)}\left(W^{(N-1)} \cdots f^{(1)}\left(W^{(1)}\boldsymbol{X}^{(0)} + \boldsymbol{b}^{(1)}\right) + \boldsymbol{b}^{(N-1)}\right) + \boldsymbol{b}^{(N)}\right), \tag{2}$$

https://doi.org/10.1038/s41567-025-03129-8

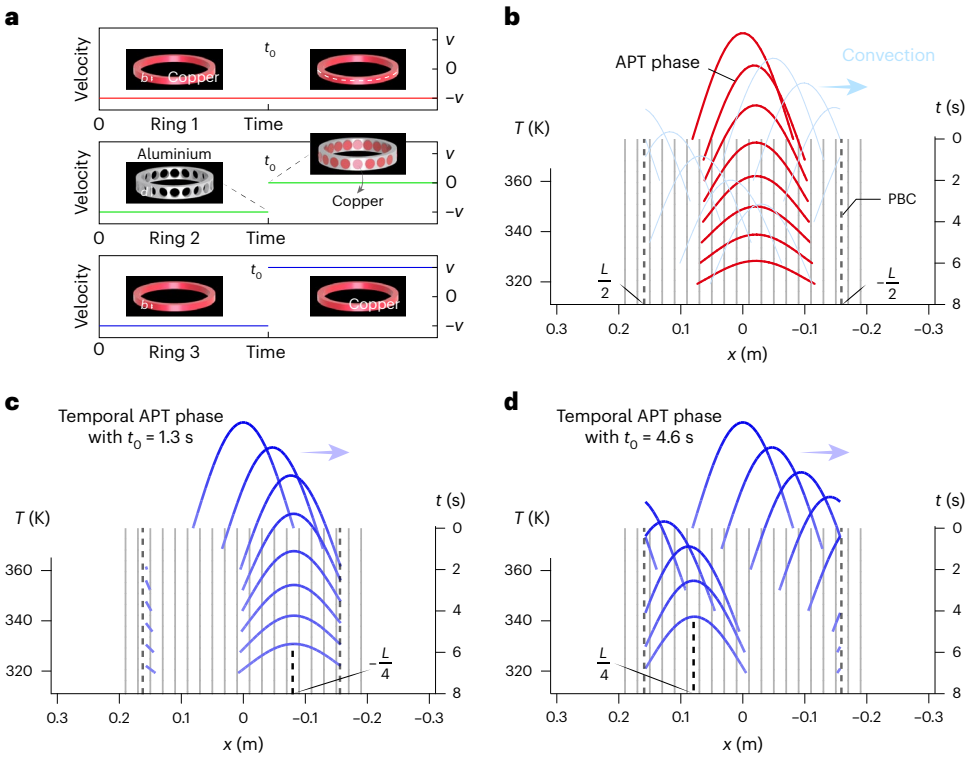

Fig. 2 | Forward heat evolution (along convection) and tunable trapping. **a**, Time-varying rotational velocities and material composition of the three rings modulate heat transfer for forward evolution and trapping. **b**, Temperature wave-packet evolution $T(x) = 40\cos(360° \times x/L) + 313.15$ K showing APT symmetry (thick line) and convection (fine line). PBC, periodic boundary conditions. **c**,**d**, Wave-packet evolution over 1/4 cycle ($t_0 = 1.3$ s) (**c**) and 3/4 cycle ($t_0 = 4.6$ s) (**d**) from $x = 0$. The top half-cycles are shown for clarity. Data from ring 1 are shown as the dashed line. The ANN accuracy is explained in Supplementary Fig. 9 (two dimensions) and Supplementary Fig. 10 (three dimensions). No error bars are shown because the outputs are deterministic simulations (non-stochastic) and have no variability to represent.

where the input layer is denoted as $\boldsymbol{X}^{(0)} = \begin{pmatrix} x_0^{\mathrm{Norm}} \\ x_T^{\mathrm{Norm}} \end{pmatrix}$. In our ANN, W and $\mathbf{b}$ represent the weight matrix and bias vector, respectively. The network contains $(N-1)$ hidden layers and f denotes the activation function applied at each layer (Supplementary Section 3).

Performance validation of temporal APT symmetry

We demonstrate the temporal APT symmetry performance through systematic simulations of forward and backward heat transport with tunable trapping. Figure 2 shows the forward heat evolution along the convection direction. The three-ring system modulates heat transfer through time-varying rotational velocities and material composition (Fig. 2a), with ring 1's velocity set as $v = 0.05$ m s^{-1}. This version uses two-dimensional rings with zero radial thickness (the three-dimensional cases are shown in Supplementary Section 4), confined by perimeter L, using a rectangular structure with periodic boundary conditions as an equivalent substitute for the circular configuration, with controllable mesh and relative tolerance settings (Supplementary Section 5).

Temperature wave packet $T(x) = 40\cos(360° \times x/L) + 313.15$ K evolves during both traditional APT-symmetric phases (enabling trapping) and convection-dominated transport phases (Fig. 2b). Precise control enables wave-packet evolution over 1/4 cycle ($t_0 = 1.3$ s) and 3/4 cycle ($t_0 = 4.6$ s) from the starting position, demonstrating forward transport and arbitrary-position trapping (Fig. 2c,d). The temperature profiles are shown in Supplementary Section 6. At t_0, the heat exchange rate shifts from $h < h^{\mathrm{EP}}$ to $h > h^{\mathrm{EP}}$, with effective thermal conductivity changing over time (Supplementary Section 7). Robustness was verified under ±10% jitter in inter-ring exchange $h(t)$, stochastic flow variations $v(r, t)$ and open boundaries to ambient 293.15 K with convective heat-transfer coefficients $h_c = 0$, 50, 100 W m^{-2} K^{-1} (Extended Data Fig. 1). Lower heat exchange rates during transport minimize heat dissipation (Supplementary Section 8), whereas increased rates during APT-symmetric phase prevent the counterconvection ring model from entering the symmetry-broken phase, ensuring effective heat trapping. We also examined a minimalist variant that holds the ring rotations fixed (ring 1, $-v$; ring 2, 0; ring 3, $+v$) and modulating only the middle ring to drive $h(t)$ across the EP threshold h^{EP}; a side-by-side comparison is provided in Supplementary Section 9. Beyond one-dimensional paths, we generalize temporal APT to a two-dimensional planar domain by scripting tangential transport and a subsequent radially directed trapping (Extended Data Fig. 2). Beyond ring geometries, we demonstrate the programmable steering of a temperature profile along a curved, S-shaped track with obstacle bypass under the same temporal APT protocol (Extended Data Fig. 3), elevating the scheme from one-dimensional transport to spatial manipulation.

Figure 3 shows an extension of this capability to backward heat evolution against convection direction. Through appropriate velocity and material design of rings 2 and 3, the temperature wave packet propagates opposite to the convection flow and maintains the trapping capability at desired locations. Wave-packet evolution over 1/4 cycle ($t_0 = 1.5$ s) and 1/2 cycle ($t_0 = 2.5$ s) demonstrates backward transport (compared with the convection-dominated phase shown in Fig. 3b) with equivalent precision to forward cases (Fig. 3c,d).

The experimental setup consisted of four integrated components (Methods): time-varying metamaterials, a pneumatic actuator, a motor-driven rotation module and an electronic control module (Fig. 4a). The pneumatic actuator switched the embedded materials within an aluminium alloy ring between air and copper at predetermined times t_0. Thermally conductive silicone grease applied at the ring inter-

https://doi.org/10.1038/s41567-025-03129-8

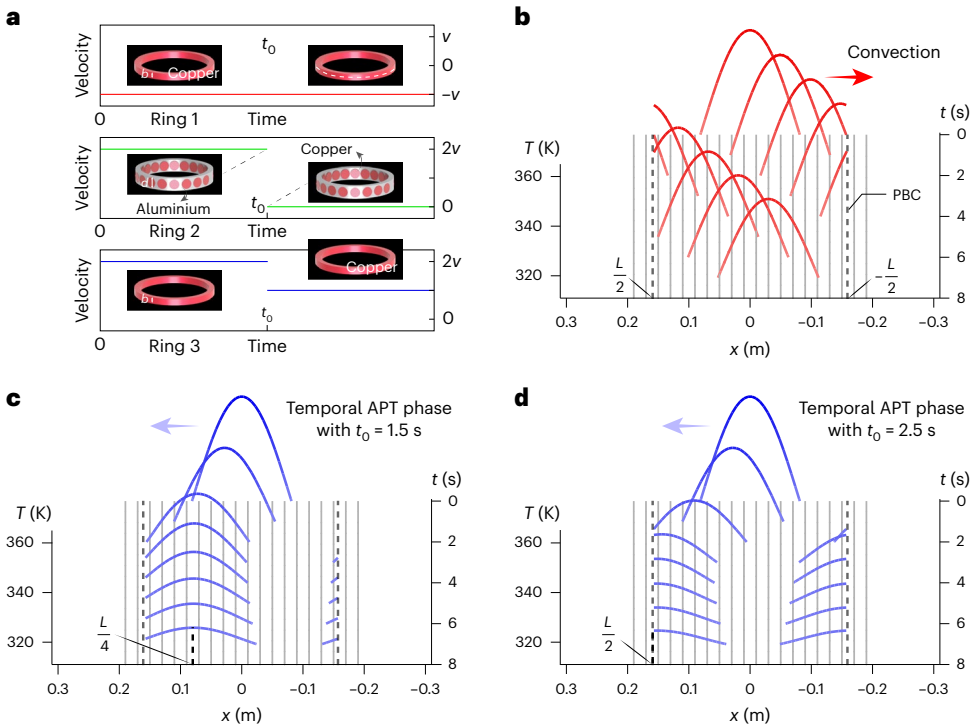

Fig. 3 | Backward heat evolution (against convection) and tunable trapping. **a**, Time-varying rotational velocities and material composition of the three rings modulate heat transfer for backward evolution and trapping. **b**, Temperature wave-packet evolution $T(x) = 40\cos(360° \times x/L) + 313.15$ K showing convection. **c**,**d**, Wave-packet evolution over 1/4 cycle ($t_0 = 1.5$ s) (**c**) and 1/2 cycle ($t_0 = 2.5$ s) (**d**) from $x = 0$. The top half-cycles are shown for clarity. Data from ring 1 are shown as the dashed line. No error bars are shown because the outputs are deterministic simulations (non-stochastic) and have no variability to represent.

faces enhanced thermal contact and reduced inter-ring thermal resistance (Extended Data Fig. 4). A small residual resistance is unavoidable, however. Its magnitude and impact on the temporal APT performance are quantified and discussed in Extended Data Fig. 5.

We demonstrated (the simulation results are provided in Supplementary Section 10) temporal APT symmetry control by trapping thermal energy at designated positions in ring 1—1/3-cycle and 2/3-cycle distances from the initial heating location (marked as position 0). A hot-air gun (473.15 K) continuously heated position 0 for 45 s (Methods discusses how the experimental initialization informs our modelling assumptions) and programmed switching times ($t_0 = 1.8$ s for 1/3-cycle trapping and $t_0 = 4.3$ s for 2/3-cycle trapping) synchronized ring rotations with actuator motion according to the temporal APT protocol (Fig. 2a).

Contact thermal resistance delayed dynamic equilibrium establishment by ~30 s despite silicone grease treatment. Temperature measurements via infrared camera revealed successful forward trapping along the convection direction: at $t_0 = 1.8$ s, thermal energy propagated with convection and localized at the 1/3-cycle position, which stabilized at 30.5 °C and maintained rotation, with heating position and 1/2-cycle position reaching 25.5 °C and 28.0 °C, respectively. For $t_0 = 4.3$ s trapping, thermal transport continued along the convection flow to the 2/3-cycle location, achieving the maximum temperature (30.5 °C), whereas 0-cycle and 1/2-cycle positions stabilized at 26.0 °C and 27.0 °C, respectively (Fig. 4b,c). Here the initial time point ($t = 0$) was defined as the moment when the position of the maximum temperature first crossed the designated trapping location.

To demonstrate counterintuitive thermal transport against convection, we implemented temporal APT symmetry, with the settings shown in Fig. 3a. Using identical heating conditions but modified switching protocols, thermal energy propagated backwards against the rotation direction to the designated trapping positions. For backward trapping at the 1/3-cycle position ($t_0 = 2.1$ s), the thermal wave packet moved against the convection flow before localizing at the target location, achieving a maximum temperature of 28.0 °C, whereas the heating position and 1/2-cycle position stabilized at 27.0 °C and 27.0 °C, respectively. Similarly, backward trapping at the 2/3-cycle position ($t_0 = 3.5$ s) demonstrated thermal energy transport opposing the rotation direction, with the target location reaching 27.0 °C compared with 26.0 °C and 26.0 °C at the 0-cycle and 1/2-cycle positions, respectively.

Critically, the temporal dynamics provide compelling evidence for backward transport against convection. In forward transport cases (Fig. 4b,c), temperature oscillations exhibit a period of ~5 s (peak-to-peak interval of 10 s represents two complete cycles), indicating rapid thermal wave propagation along the convection direction. Conversely, in backward transport cases (Fig. 4d,e), the same peak-to-peak interval of 10 s corresponds to a single cycle, demonstrating that thermal waves propagate at half the speed when moving against the convection flow. This reduced propagation velocity directly confirms that thermal energy transport occurs counter to the convection. For an intuitive physical picture of the backward transport window ($t < t_0$), the finite inter-ring exchange maintains a phase-locked coupling between ring 1 ($-v$) and the counter-rotating pair ($+2v$), subtly biasing the instantaneous exchange so that phase-advanced components are preferentially retained on ring 1, whereas phase-delayed components are shed. This imbalance manifests as an effective negative advection that, within our parameter regime, outweighs the imposed convection and sets the drift's sign and reduced magnitude, in agreement with $\mathrm{Re}[\omega(t)] < 0$.

These results confirm successful bidirectional thermal transport control through temporal APT symmetry engineering, enabling thermal wave-packet manipulation both along and against convection flow—a capability fundamentally distinct from conventional thermal management approaches (Fig. 4d,e).

https://doi.org/10.1038/s41567-025-03129-8

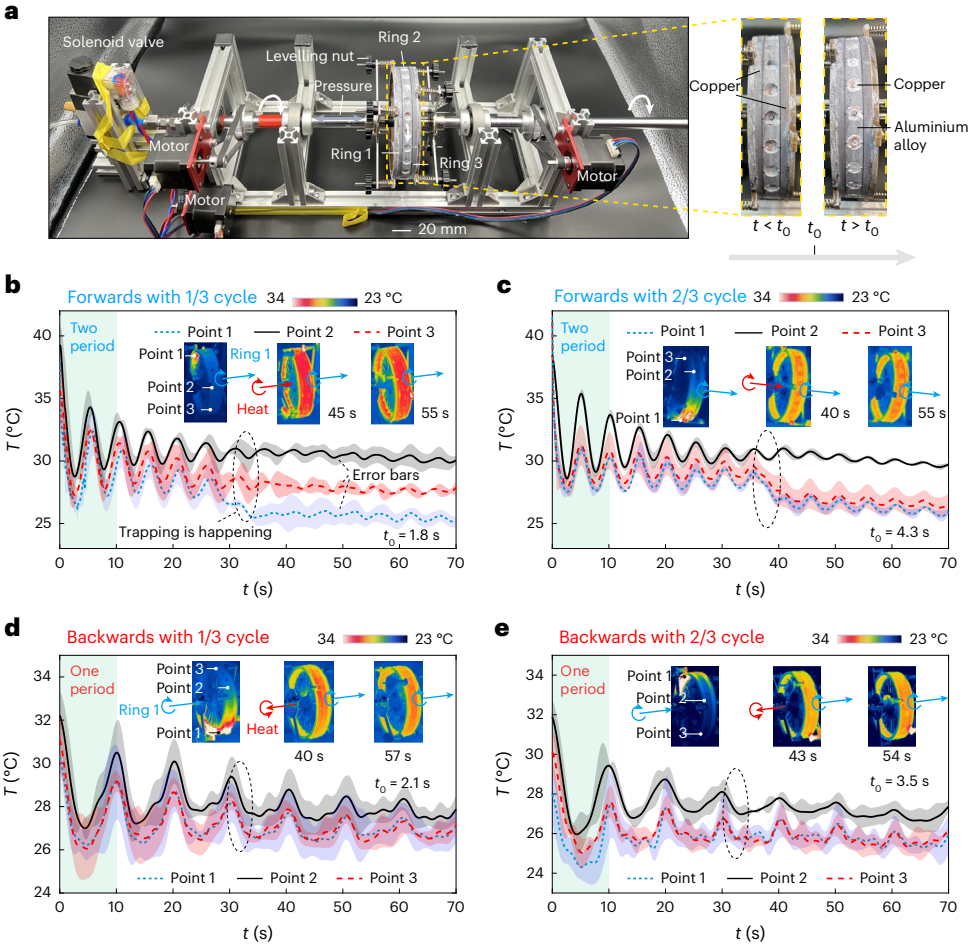

Fig. 4 | Experimental demonstration of counterintuitive thermal transport via temporal APT symmetry. a, Experimental setup featuring two copper rings exchanging heat through an aluminium alloy ring with a switchable embedded material. A pneumatic actuator switches the embedded component between air and copper at predetermined times t_0, whereas three motors independently rotate the rings. Temperature evolution is measured at three points (positions indicated) with thermal profiles. **b**,**c**, Forward evolution and trapping at 1/3-cycle (**b**) and 2/3-cycle (**c**) positions from the heating point, with switching times $t_0 = 1.8$ s and $t_0 = 4.3$ s, respectively. The results depict the temporal evolution of temperature measured at positions 0 (point 1), 1/3 (point 2) and 1/2 (point 3) of a cycle (**b**), and at positions 0 (point 1), 1/2 (point 3) and 2/3 (point 2) of a cycle (**c**). **d**,**e**, Backward evolution and trapping at 1/3-cycle (**d**) and 2/3-cycle (**e**) positions, with switching times $t_0 = 2.1$ s and $t_0 = 3.5$ s, respectively. Temperature profiles show the transition from propagating to trapped states following temporal APT symmetry switching. The results depict the temporal evolution of temperature measured at positions 0 (point 1), 1/3 (point 2) and 1/2 (point 3) of a cycle (**d**), and at positions 0 (point 1), 1/2 (point 3) and 2/3 (point 2) of a cycle (**e**). Error bars (shaded regions) indicate one standard deviation based on three independent measurements. All experimental data shown are smoothed; raw data are provided in Supplementary Fig. 34.

Conclusion and outlook

In conclusion, we have introduced the temporal modulation of non-Hermitian phase transitions as a programmable means to dynamically control diffusive transport. We realized this paradigm in a three-ring thermal metadevice, where time-modulated couplings between elements enable active control over the system's temporal APT symmetry. This moves beyond static phase classification, allowing the complete scripting of thermal transport trajectories. Our experiments demonstrate unprecedented command over thermal energy: catching a profile in transit, driving it forward with convection, reversing it against the flow or trapping it at any desired location. Such capability mirrors the optical-tweezers-based manipulation of dielectric particles[48], but here programmable phase transitions replace laser-induced potentials, enabling heat control in diffusive media via a genuinely non-Floquet route. The dynamics rely on non-periodic, order-sensitive and non-commutative time evolution across EPs (Extended Data Fig. 6 and Supplementary Section 2).

The practical implications are immediate and substantial. In microelectronics, our approach enables intelligent thermal circuits that can actively guide cooling energy to critical processing units during peak operations. In renewable energy, the dynamic shaping of temperature gradients can overcome static efficiency limits in thermoelectric devices. This potential is underpinned by the framework's remarkable robustness, which is confirmed against wide-ranging initial conditions (non-uniformity (Supplementary Section 8) and amplitude, wavelength and waveform (Supplementary Section 11)), system size (Supplementary Sections 12 and 13), convective intensity (Supplementary Fig. 29) and material properties (Supplementary Fig. 30), further validated by a proof-of-concept experiment achieving an ~5-K enhancement in targeted cooling (Extended Data Fig. 7 and Supplementary Section 14). We also introduce and quantify an application-oriented figure of merit—the effective transport distance (distance travelled before the peak amplitude drops to 5% of its initial excess; Supplementary Fig. 33).

The implications of this temporal paradigm, however, extend far beyond thermal science. It provides a universal blueprint for four-dimensional (space-time) control. Imagine sculpting the refractive index and gain/loss in photonic systems in real time to catch, hold and release light pulses at will, creating the ultimate optical memory. Envision dynamically tuning acoustic metamaterials to trap a vibrational shockwave before it reaches a sensitive component, or steering

spin waves in magnonic devices with temporal precision. Ultimately, this work redefines the objective of metamaterial design: the goal is no longer to engineer a static response in space but to command the dynamic evolution of energy in time. This heralds a new era of intelligent, four-dimensional control over wave and energy transport.

Online content

Any methods, additional references, Nature Portfolio reporting summaries, source data, extended data, supplementary information, acknowledgements, peer review information; details of author contributions and competing interests; and statements of data and code availability are available at https://doi.org/10.1038/s41567-025-03129-8.

References

1. Gross, D. J. The role of symmetry in fundamental physics. *Proc. Natl Acad. Sci. USA* **93**, 14256–14259 (1996).
2. Bender, C. M. & Boettcher, S. Real spectra in non-Hermitian Hamiltonians having PT symmetry. *Phys. Rev. Lett.* **80**, 5243–5246 (1998).
3. Bergholtz, E. J., Budich, J. C. & Kunst, F. K. Exceptional topology of non-Hermitian systems. *Rev. Mod. Phys.* **93**, 15005 (2021).
4. Heiss, W. D. The physics of exceptional points. *J. Phys. A: Math. Theor.* **45**, 444016 (2012).
5. Miri, M. A. & Alù, A. Exceptional points in optics and photonics. *Science* **363**, eaar7709 (2019).
6. Özdemir, S. K., Rotter, S., Nori, F. & Yang, L. Parity–time symmetry and exceptional points in photonics. *Nat. Mater.* **18**, 783–798 (2019).
7. Chen, W. J., Özdemir, S. K., Zhao, G. M., Wiersig, J. & Yang, L. Exceptional points enhance sensing in an optical microcavity. *Nature* **548**, 192–196 (2017).
8. Feng, L., Wong, Z. J., Ma, R. M., Wang, Y. & Zhang, X. Single-mode laser by parity–time symmetry breaking. *Science* **346**, 972–975 (2014).
9. Zeng, Y. Q. et al. Electrically pumped topological laser with valley edge modes. *Nature* **578**, 246–250 (2020).
10. Zhang, J. et al. A phonon laser operating at an exceptional point. *Nat. Photon.* **12**, 479–484 (2018).
11. Zhang, X. Y. et al. Symmetry-breaking-induced nonlinear optics at a microcavity surface. *Nat. Photon.* **13**, 21–24 (2019).
12. Makris, K. G., El-Ganainy, R., Christodoulides, D. N. & Musslimani, Z. H. Beam dynamics in PT symmetric optical lattices. *Phys. Rev. Lett.* **100**, 103904 (2008).
13. Feng, L., El-Ganainy, R. & Ge, L. Non-Hermitian photonics based on parity–time symmetry. *Nat. Photon.* **11**, 752–762 (2017).
14. El-Ganainy, R. et al. Non-Hermitian physics and PT symmetry. *Nat. Phys.* **14**, 11–19 (2018).
15. Zhu, X. F., Ramezani, H., Shi, C. Z., Zhu, J. & Zhang, X. PT-symmetric acoustics. *Phys. Rev. X* **4**, 031042 (2014).
16. Zhang, Z., Delplace, P. & Fleury, R. Superior robustness of anomalous non-reciprocal topological edge states. *Nature* **598**, 293–297 (2021).
17. Han, Y. C. et al. Bound chiral magnonic polariton states for ideal microwave isolation. *Sci. Adv.* **9**, eadg4730 (2023).
18. Wu, J. H., Artoni, M. & La Rocca, G. C. Non-Hermitian degeneracies and unidirectional reflectionless atomic lattices. *Phys. Rev. Lett.* **113**, 123004 (2014).
19. Peng, P. et al. Anti-parity–time symmetry with flying atoms. *Nat. Phys.* **12**, 1139–1145 (2016).
20. Konotop, V. V. & Zezyulin, D. A. Odd-time reversal symmetry induced by an anti-PT-symmetric medium. *Phys. Rev. Lett.* **120**, 123902 (2018).
21. Azizi, P. et al. Lattice materials with topological states optimized on demand. *Proc. Natl Acad. Sci. USA* **122**, e2506787122 (2025).
22. Qi, M. H. et al. Geometric phase and localized heat diffusion. *Adv. Mater.* **34**, 2202241 (2022).
23. Qi, M. H. et al. Observation of high-decay-rate topological corner states in diffusive thermal metamaterials. *Phys. Rev. Lett.* **135**, 096604 (2025).
24. Li, Y. et al. Anti-parity–time symmetry in diffusive systems. *Science* **364**, 170–173 (2019).
25. Xu, G. et al. Non-Hermitian chiral heat transport. *Phys. Rev. Lett.* **130**, 266303 (2023).
26. Cao, P. C. et al.Observation of parity–time symmetry in diffusive systems. *Sci. Adv.* **10**, eadn1746 (2024).
27. Xu, G. et al. Hydrodynamic moiré superlattice. *Science* **386**, 1377–1383 (2024).
28. Xu, G. et al. Diffusive topological transport in spatiotemporal thermal lattices. *Nat. Phys.* **18**, 450–456 (2022).
29. Xu, G. Q. et al. Observation of Weyl exceptional rings in thermal diffusion. *Proc. Natl Acad. Sci. USA* **119**, e2110018119 (2022).
30. Xu, G. Q., Li, Y., Li, W., Fan, S. H. & Qiu, C.-W. Configurable phase transitions in a topological thermal material. *Phys. Rev. Lett.* **127**, 105901 (2021).
31. Yang, F. B. et al. Controlling mass and energy diffusion with metamaterials. *Rev. Mod. Phys.* **96**, 015002 (2024).
32. Li, Y. et al. Transforming heat transfer with thermal metamaterials and devices. *Nat. Rev. Mater.* **6**, 488–507 (2021).
33. Zhu, C. L., Bamidele, E. A., Shen, X. Y., Zhu, G. M. & Li, B. W. Machine learning aided design and optimization of thermal metamaterials. *Chem. Rev.* **124**, 4258–4331 (2024).
34. Liu, Z. F. et al. Topological thermal transport. *Nat. Rev. Phys.* **6**, 554–565 (2024).
35. Jin, P. et al. Tunable liquid-solid hybrid thermal metamaterials with a topology transition. *Proc. Natl Acad. Sci. USA* **120**, e2217068120 (2023).
36. Jin, P. et al. Deep learning-assisted active metamaterials with heat-enhanced thermal transport. *Adv. Mater.* **36**, 2305791 (2024).
37. Li, Y., L. Xu & Qiu. C.-W. *Thermal Metamaterials: Controlling the Flow of Heat* (World Scientific, 2025).
38. Tirole, R. et al. Double-slit time diffraction at optical frequencies. *Nat. Phys.* **19**, 999–1002 (2023).
39. Sapienza, R. Splitting light pulses. *Nat. Photon.* **19**, 551–552 (2025).
40. Liu, Z. F. et al. Topology in thermal, particle, and plasma diffusion metamaterials. *Chem. Rev.* **125**, 8655–8730 (2025).
41. Fan, C. Z., Wu, C.-L., Wang, Y., Wang, B. & Wang, J. Thermal metamaterials: from static to dynamic heat manipulation. *Phys. Rep.* **1077**, 1–111 (2024).
42. Dai, G. L. et al. Controlling transient and coupled diffusion with pseudoconformal mapping. *Proc. Natl Acad. Sci. USA* **122**, e2511708122 (2025).
43. Lei, M. et al. Reconfigurable, zero-energy, and wide-temperature loss-assisted thermal nonreciprocal metamaterials. *Proc. Natl Acad. Sci. USA* **121**, e2410041121 (2024).
44. Tan, H. H. et al. Bioinspired energy-free temperature gradient regulator for significant enhancement of thermoelectric conversion efficiency. *Proc. Natl Acad. Sci. USA* **122**, e2424421122 (2025).
45. Lindner, N. H., Refael, G. & Galitski, V. Floquet topological insulator in semiconductor quantum wells. *Nat. Phys.* **7**, 490–495 (2011).
46. Rudner, M. S. & Lindner, N. H. Band structure engineering and non-equilibrium dynamics in Floquet topological insulators. *Nat. Rev. Phys.* **2**, 229–244 (2020).
47. Lei, M. et al. Quantum thermalization and Floquet engineering in a spin ensemble with a clock transition. *Nat. Phys.* **21**, 1196–1202 (2025).
48. Ashkin, A., Dziedzic, J. M., Bjorkholm, J. E. & Chu, S. Observation of a single-beam gradient force optical trap for dielectric particles. *Opt. Lett.* **11**, 288–290 (1986).

Methods

Finite-element simulations

We utilize the COMSOL Multiphysics software to simulate the evolution of the physical field within the structure. Before initiating the simulation, we specify the model's dimensions, focusing on both two-dimensional and three-dimensional cases, and select the transient process for analysis. To study heat transfer in rotating rings, we use the 'Solid and Fluid Heat Transfer' module. Initially, we define the size and material parameters for the three-ring model within the 'Component' module. For the two-dimensional case (Supplementary Fig. 1a), each ring is treated equivalently as a rectangle, where length L represents the circumference of the ring with radius $R_{ring} = 0.05$ m. The width of the rectangle corresponds to the axial size of the rings, with the outer rings having a width $b = 0.005$ m and the middle ring a width $d = 0.01$ m. In this two-dimensional model, the radial thickness of all three rings is considered to be zero. A series of equally spaced circles, each with a radius R of 0.004 m and separated by 0.01 m, are positioned along the central axis of the middle ring, extending along the length of the rectangle. In particular, the centre of the leftmost (rightmost) circle is positioned 0.007 m from the left (right) boundary for geometric approximation.

When defining the material parameters for the three rings, the outer rings are composed of copper, with a thermal conductivity of 400 W m^{-1} K^{-1}, a heat capacity of 385 J kg^{-1} K^{-1} and a mass density of 8900 kg m^{-3}. The middle ring, excluding the circles, is made of aluminium alloy, which has a thermal conductivity of 180 W m^{-1} K^{-1}, a heat capacity of 880 J kg^{-1} K^{-1} and a mass density of 2,700 kg m^{-3}. Initially, the circles are filled with air, characterized by a thermal conductivity of 0.026 W m^{-1} K^{-1}, a heat capacity of 1,005 J kg^{-1} K^{-1} and a mass density of 1.2 kg m^{-3}. After time t_0, the circles are replaced with copper, as specified by the program instruction: if ($t < t_0$, 0.026, 400) (using thermal conductivity as an example). Here t represents the system's evolution time. The system's left and right boundaries are set with periodic boundary conditions, whereas the upper and lower boundaries are thermally insulated. The initial temperature distribution (represented by colour in Supplementary Fig. 1) is given by $T(x) = 40\cos(360° \times x/L) + 313.15$ K. In the three-dimensional case, the primary difference lies in the radial thickness of the rings, which is set to 0.008 m. The inner and outer radii of the rings are 0.05 m and 0.058 m, respectively. We then define the motion of the three rings. Throughout the process, ring 1 maintains a constant velocity of 0.05 m s^{-1}. Ring 2 moves at 0.05 m s^{-1} before time t_0, and comes to rest afterwards. Similarly, ring 3 moves at 0.05 m s^{-1} before t_0, but reverses direction to −0.05 m s^{-1} after t_0. In the three-dimensional case, ring 1 maintains a constant angular velocity ω of 1 rad s^{-1} throughout. Ring 2 has an angular velocity of 1 rad s^{-1} before t_0 and reduces to 0 rad s^{-1} thereafter. For ring 3, the angular velocity starts at 1 rad s^{-1} before t_0, but switches to −1 rad s^{-1} afterwards. In three dimensions, we build the full 360° annular geometry, so the azimuthal periodicity is intrinsic and no periodic boundary pairs are required. The initial condition $T(\theta) = 40\cos\theta + 313.15$ K is 2π periodic (represented by colour in Supplementary Fig. 1). All external (environment-facing) boundaries—inner/outer cylindrical surfaces and axial end faces—are thermally insulated ($\mathbf{n}\cdot(-\kappa\nabla\mathbf{T}) = \mathbf{0}$). Internal interfaces between rings and inserts use continuity (perfect thermal contact).

Experimental realization

The construction of the entire experimental setup can be divided into four parts: metamaterial processing, pneumatic device design, circuit control module and motor-driven rotation module.

Metamaterial processing. We utilized computerized numerical control technology to machine two copper rings with an inner radius of 0.058 m, an outer radius of 0.063 m and an axial thickness of 0.005 m. The copper material has a thermal conductivity of 400 W m^{-1} K^{-1}, a heat capacity of 385 J kg^{-1} K^{-1} and a mass density of 8,900 kg m^{-3}. Additionally, we three-dimensionally printed an aluminium alloy 6061 ring, which has an inner radius of 0.058 m, an outer radius of 0.063 m and an axial thickness of 0.01 m. The aluminium alloy has a thermal conductivity of 180 W m^{-1} K^{-1}, a heat capacity of 880 J kg^{-1} K^{-1} and a mass density of 2,700 kg m^{-3}. These aluminium rings feature 24 evenly spaced circular air holes along the tangential direction. The air holes have a radial depth (the radial direction of the aluminium alloy ring) of 5 mm and a diameter of 8 mm. In subsequent stages, the air-hole regions are switched to copper columns. Quartz tubes (diameter of 3 mm, thermal conductivity of 1.3 W m^{-1} K^{-1}, density of 2,650 kg m^{-3} and heat capacity of 740 J kg^{-1} K^{-1}) are used to mechanically drive the circular copper columns (8 mm in diameter and 5 mm in height). We installed 24 cylinders radially along the inner circumference of the middle ring to switch the material composition of the air-hole regions. Pneumatic pressure is used to push the copper columns outwards, whereas the columns are retracted by the spring force.

Pneumatic device design. A pneumatic device has been designed to switch the material configuration of the aluminium alloy ring. An air compressor (with a capacity of 5 l) increases the pressure of low-pressure air to higher pressures through air compression. The compressed air serves as the driving source for pneumatic devices such as pneumatic pumps. The switch of the air compressor is a red button (Supplementary Fig. 2, bidirectional arrow). When pulled outwards, it allows air to flow into the compressor. Pushing the red button inwards halts the air intake. Below the red button, a black box contains a screw that adjusts the pressure within the cylinder, with a maximum threshold of 0.6 MPa. However, 0.6 MPa is sufficiently high for our needs; therefore, a pressure-reducing valve is used to further decrease the output pressure. When the valve is loosened, the output pressure is zero; as the valve is tightened, the pressure gradually increases, eventually reaching 0.25 MPa, which meets our requirements. Finally, the exhaust pipe's outlet is inserted into the air circuit for switching the material component of the central ring (the pipe is directly inserted, and when removing, the connector must be pressed to detach). A blue button controls the air circuit: pressing it allows air to flow, and releasing it stops the airflow. This blue button can be used to test the entire air circuit, ensuring that the material switching occurs smoothly. Proper sealing between the various air circuits is essential to maintain airtightness.

Circuit control module. The circuit module (Supplementary Fig. 3) is designed to control the mechanical rotation and material switching of the metamaterial. Stepper motors are used to drive the mechanical rotation of the metamaterial. The microcontroller unit serves as the central control system, enabling motor rotation with time-responsive characteristics. Pneumatic devices are used to control the material switching of the metamaterial. The control system within the microcontroller unit operates relays to control the electromagnetic valve's on/off state, supplying power to the valve at specified moments, thereby allowing pneumatic pressure to lift the copper within the central ring and fill the air cavities in the aluminium alloy ring. The entire program is stored on a USB drive, which is connected to the programmer via a USB-to-TTL module, as the microcontroller operates with TTL-level signals. The PCB acts as a carrier, with connections made using DuPont wires. A 220-V a.c. power supply is converted to 24-V d.c. to power the stepper motor driver, whereas a 3.3-V power supply provides energy to the circuit board. The control module includes four buttons: button 1 selects different modules (switching time, rotational speed and working mode); buttons 2 and 3 adjust the switching time and rotational speed. Button 2 allows switching between the working modes, including 0 (no material switching in the central ring), 1 (neutral position) and 2 (material switching in the central ring). Button 4 starts and stops the program. The display module is an OLED screen: the first line shows the electromagnetic valve's operation time (that is, the switching time),

the second line displays the motor's rotation speed and the third line shows the current working mode.

Motor-driven module. The specific settings for the motors match those in the three-dimensional simulations. We use synchronous belt and gear systems to control the rotation of the stainless steel tubes, which, in turn, drive the rotation of the rings. The medium that facilitates the rotation of the copper rings are the wooden support structures. These support structures extend three wooden prongs that make contact with the copper rings. The copper rings and the prongs are bonded using 810 adhesive, aligned and then held in place for 10 s. Additionally, a limit stop is incorporated to prevent axial motion of the ring during rotation, thereby ensuring proper compression and contact between the rings.

Linking experimental initialization to modelling assumptions

In the experiments, we start from a localized hotspot created by the hot-air gun at position 0. Owing to rapid tangential advection in copper and diffusion, this localized profile relaxes within a few seconds to the first-harmonic-dominated state along the ring. To make this connection explicit, we performed finite-element simulations of the experimental sample in which all the rings are locally heated for 15 s by a tangentially confined boundary heat flux that emulates the hot-air nozzle: $q(\theta) = -230\cos(8\theta - \pi)$W, where $-\pi/16 \le \theta \le \pi/16$, applied for 15 s. Starting from a localized hotspot, the tangential temperature profile evolves into a broad (Extended Data Fig. 8), first-harmonic-like waveform by the end of the 15 s of heating (not to mention 45 s), matching the trend observed experimentally (see Fig. 4). This validates that the idealized $\cos\theta$ initial condition used in our simulations is an appropriate and accurate approximation for the experimentally realized state at the time we trigger the temporal APT protocol. Consistent with this observation, our robustness tests in Supplementary Figs. 24–26 show that the temporal APT performance—propagation, trapping location and timing—is insensitive to the initial waveform, amplitude and wavelength. Thus, starting from a localized hotspot is, in practice, a stronger test that leads to the same trapping outcomes.

Ambient laboratory conditions

The ambient laboratory temperature was actively controlled and documented because the environment serves as a large thermal reservoir that sets the cooling rate of the system. All the measurements were repeated three times to determine the error bars, and for each panel in Fig. 4, the three runs were carried out at the same room-temperature set point. The temperature near the setup was monitored with an infrared camera (0.1 °C precision). To exploit naturally stable conditions, the data in Fig. 4 were collected in mid-June (Shanghai) between 13:00 and 17:00, when the outdoor temperature is relatively steady (>25 °C); the air conditioning maintained the room at approximately 24 °C for each repetition of a given panel. The specific per-run ambient temperatures are listed in Extended Data Table 1 and meet the requirement of constancy across repetitions. To suppress forced convection from the air conditioner, we used a two-stage protocol: (1) the unit was turned on well before data collection and the room temperature was monitored until it stabilized; (2) the unit was then turned off, and measurements were taken afterwards. This removes active air currents and allows the setup to evolve in a quiescent room. Combined with the temperature-control procedure above, this establishes stable laboratory conditions and limits environmental drift during acquisition.

Data smoothing algorithm

In our analysis, we adopted frequency-domain filtering using the fast Fourier transform (FFT). The FFT represents a discrete-time series $x_n (n = 0 \ldots N-1)$ as a superposition of harmonic modes:

$$X_k = \sum_{n=0}^{N-1} x_n e^{-i2\pi kn/N},$$

where X_k is the spectral amplitude at frequency $f_k = k/(N\Delta t)$, with Δt being the sampling interval and N, the window size. Data smoothing is implemented by suppressing the Fourier components with $f_k > f_c$, where f_c is the cut-off frequency. The choice of f_c determines the balance between noise removal and signal fidelity: lowering f_c efficiently suppresses high-frequency fluctuations but risks attenuating sharp transitions and distorting peak shapes, whereas a higher f_c preserves detailed structures at the expense of residual noise. The window length N introduces another trade-off. Since the frequency resolution is $\Delta f = 1/(N\Delta t)$, a larger N improves the spectral selectivity and, thus, enhances the ability to distinguish closely spaced modes. However, increasing N also broadens the effective temporal averaging, thereby reducing time localization and potentially smearing peak timing. Conversely, a small N yields better temporal accuracy but coarse spectral resolution. With an appropriate choice of cut-off frequency and window size, FFT can accurately preserve both period and peak positions. To demonstrate this, we present the smoothed data alongside the raw measurements in Supplementary Fig. 34f. As shown, there is an agreement in both period and peak positions between the raw data (blue dots) and the FFT-filtered result (red line).

Effect of thermal grease on heat exchange in copper rings

We designed two sets of experiments to quantitatively characterize the effect of thermal grease on heat exchange in copper rings.

In experiment 1, two copper rings were aligned and stacked. A hot-air gun (set to a working temperature of 200 °C) was used to heat the upper copper ring for 15 s. The heating position is marked in Extended Data Fig. 4. After removing the hot-air gun, the two copper rings were allowed to cool naturally. The heat exchange between the two rings was characterized by monitoring the temperature evolution over time at two specific positions: one on the upper copper ring (at point 1) and one on the lower copper ring (at point 2). Three datasets were collected under the same experimental conditions.

In experiment 2, the conditions were modified by applying a layer of thermal grease (thermal conductivity, 1.15 W m^{-1} K^{-1}) at the contact area between the two copper rings. Other experimental setup and procedure remained the same as that in experiment 1. Again, three datasets were measured.

For both experiments, we calculated the average temperature and standard deviation of the three sets of measurements as follows:

1. Average temperature $\overline{T(t=t_0)}$ from point 1 or point 2 at moment $t = t_0$:

$$\overline{T(t=t_0)} = \frac{1}{n}\sum_{i=1}^{n} T_i(t=t_0).$$

2. Standard deviation $s_T(t=t_0)$ from point 1 or point 2 at moment $t = t_0$:

$$s_T(t=t_0) = \sqrt{\frac{1}{n-1}\sum_{i=1}^{n}[T_i(t=t_0) - \overline{T(t=t_0)}]^2}.$$

3. Measured temperature $T(t=t_0)$ from point 1 or point 2 at moment $t = t_0$:

$$T(t=t_0) = \overline{T(t=t_0)} \pm s_T(t=t_0).$$

Here $i = 1, 2, 3$ marks the three sets of measurements. $T_i(t=t_0)$ represents the measured temperature of group i from point 1 or point 2 at moment $t = t_0$. Our results demonstrate that the application of thermal grease enhanced the heat exchange capacity between the two rings, both during the 15-s heating period and the subsequent natural cooling phase up to 2 min.

Data availability

Source data are provided with this paper.

Acknowledgements
We thank H. Fang for the constructive suggestions on improving the quality of the manuscript. This work was supported by the National Natural Science Foundation of China to J.H. (12035004 and 12320101004), the Innovation Program of Shanghai Municipal Education Commission to J.H. (2023ZKZD06), the Singapore Ministry of Education to C.-W.Q. (A-8002978-00-00) and the Singapore Ministry of Education under the Academic Research Fund Tier 2 (FY2023) to G.W.H. (T2EP50124-0007).

Author contributions
P.J., C.-W.Q. and J.H. conceived the ideas. C.W. developed the theory. P.J. designed the algorithm and performed the simulations. P.J., C.W., Yuhong Z. and J.L. conducted the experiments. P.J., C.W. and Yuhong Z. performed the visualization. P.J., C.W., Yuhong Z. and S.Y. wrote the manuscript. G.W.H., C.-W.Q. and J.H. supervised the project. All authors contributed to the discussion and finalization of the manuscript.

Competing interests
The authors declare no competing interests.

Additional information
Extended data is available for this paper at https://doi.org/10.1038/s41567-025-03129-8.

Supplementary information The online version contains supplementary material available at https://doi.org/10.1038/s41567-025-03129-8.

Correspondence and requests for materials should be addressed to Cheng-Wei Qiu or Jiping Huang.

Peer review information *Nature Physics* thanks the anonymous reviewers for their contribution to the peer review of this work.

https://doi.org/10.1038/s41567-025-03129-8

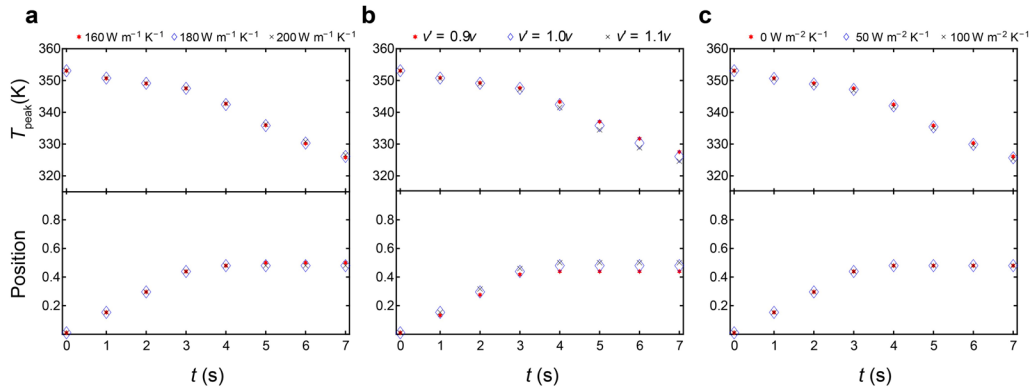

Extended Data Fig. 1 | Robustness of temporal APT symmetry to parameter jitter, stochastic flows, and boundary exchange. Top panels: peak temperature T_{peak}(K) vs time t; bottom panels: Position (normalized distance of the instantaneous peak relative to the initial location, expressed as cycle fraction) vs time t. **a**, Material-property jitter: thermal conductivity of the middle ring varied by ±10% (160, 180, 200 W m^{-1}K^{-1}). **b**, Stochastic flows: the programmed velocity of Ring 1 is perturbed by ±10% ($v' = 0.9v$, $1.0v$, $1.1v$). **c**, Uncertain boundary conditions: ambient 293.15 K with convective heat-transfer coefficients $h_c = 0$, 50, 100 W m^{-2}K^{-1}. In all cases, the protocol preserves the T_{peak} and Position trajectories within numerical tolerances, confirming stable transport and trapping under these perturbations. For this model, the switching time is $t_0 = 2.8$ s, with all other parameters identical to those in Fig. 2.

https://doi.org/10.1038/s41567-025-03129-8

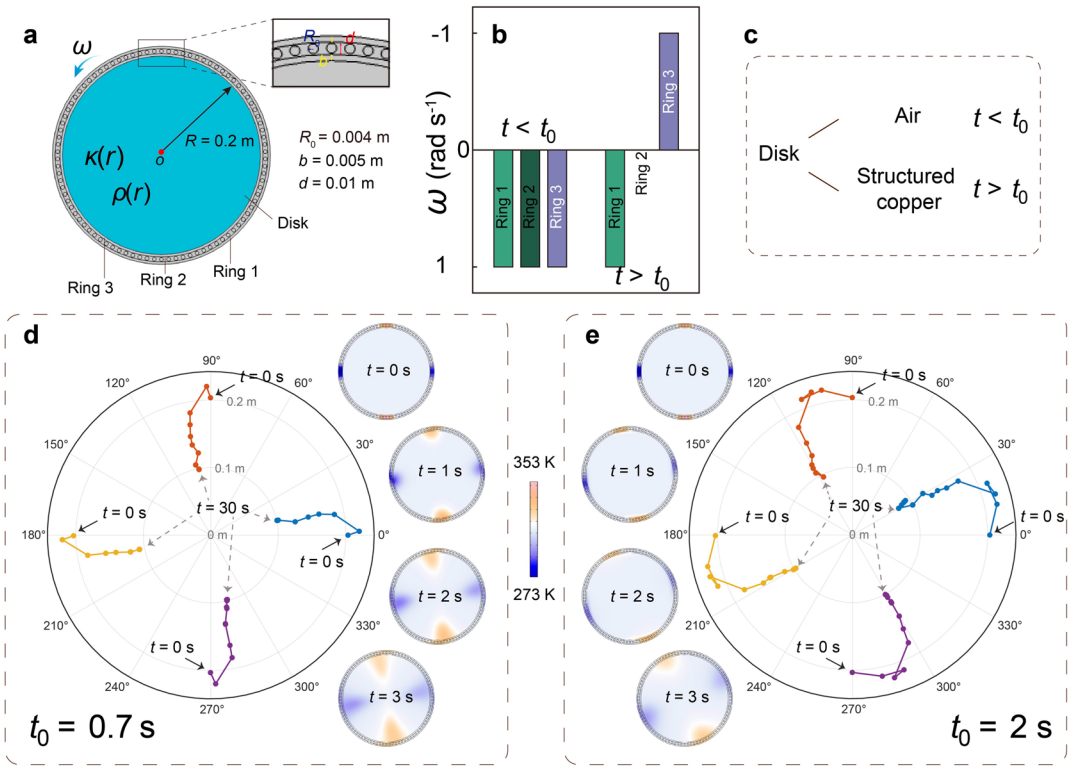

Extended Data Fig. 2 | Temporal APT on a planar disk. a, Three-ring model (inner radius $R = 0.2$ m) and concentric architecture used for tangential transport; all other parameters match Fig. 2. **b**, Ring angular velocities before and after the switching time t_0. **c**, At t_0, the hollow interior is replaced by a structured copper disk with radially graded properties, $\kappa(r) = \kappa_0 e^{-100(1-r/R)}$ and $\rho(r) = \rho_0 e^{-100(1-r/R)}$, to emulate radial drift. Here, $\kappa_0 = 400$ W m^{-1} K^{-1} and $\rho_0 = 8900$ kg m^{-3} are the thermal conductivity and density of copper. **d**-**e**, Two representative scripts ($t_0 = 0.7$ s and $t_0 = 2.0$ s): polar plots of the peak location over time and early-stage temperature profiles show controlled tangential motion, directed radial steering, and trapping at the selected polar coordinates.

https://doi.org/10.1038/s41567-025-03129-8

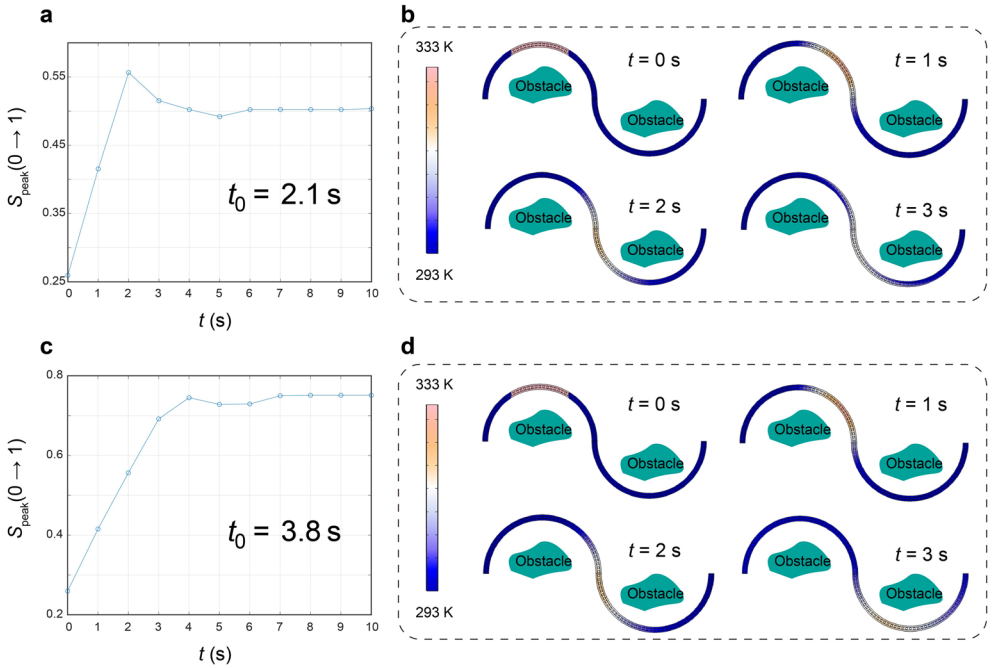

Extended Data Fig. 3 | Steering a temperature profile along an S-shaped track to bypass obstacles via temporal APT control. Passive obstacles are placed between the rails. The upper rail centerline is parameterized by $S \in [0,1]$, with $S = 0$ at the left end and $S = 1$ at the right end. The initial temperature distribution along the track at $t = 0$ s is visualized by the color map. **a**, Normalized peak position $S_{peak}(0 \to 1)$ along the upper rail centerline vs time for $t_0 = 2.1$ s, showing evolution from ≈ 0.25 to ≈ 0.50. **b**, Temperature snapshots ($t = 0$–3 s) on both semicircular rails with obstacles, illustrating guided motion around obstacles from a cosine-modulated initial condition. **c**, Same as (**a**) for $t_0 = 3.8$ s; the peak advances from ≈ 0.25 to ≈ 0.75. **d**, Snapshots ($t = 0$–3 s) for $t_0 = 3.8$ s. Geometry: two semicircular rails concatenated into an S-track; inner radius $R = 0.2$ m; rings rotate at $|\omega| = 1$ rad s^{-1}; all other parameters match Fig. 2.

https://doi.org/10.1038/s41567-025-03129-8

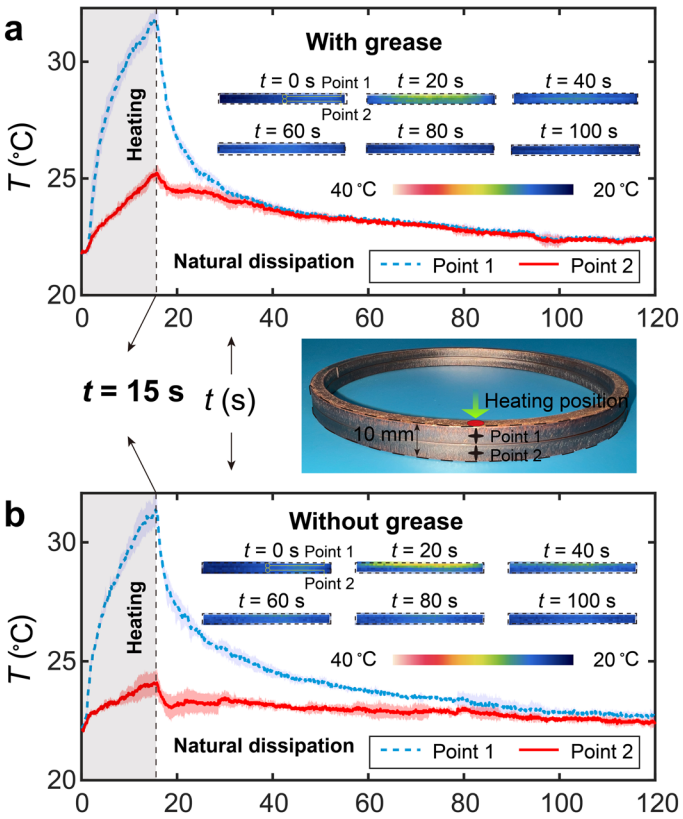

Extended Data Fig. 4 | Effect of thermal grease on heat exchange in copper rings. a, Time-dependent temperature evolution at points 1 and 2 on two copper rings (with thermal grease). **b**, Time-dependent temperature evolution at points 1 and 2 on two copper rings (without thermal grease). The insets display the temperature profiles (comes from the second measurement) of both copper rings (with/without grease) over time. Error bars (shaded areas) represent one standard deviation from the mean. The middle inset displays the picture of our experimental setup.

https://doi.org/10.1038/s41567-025-03129-8

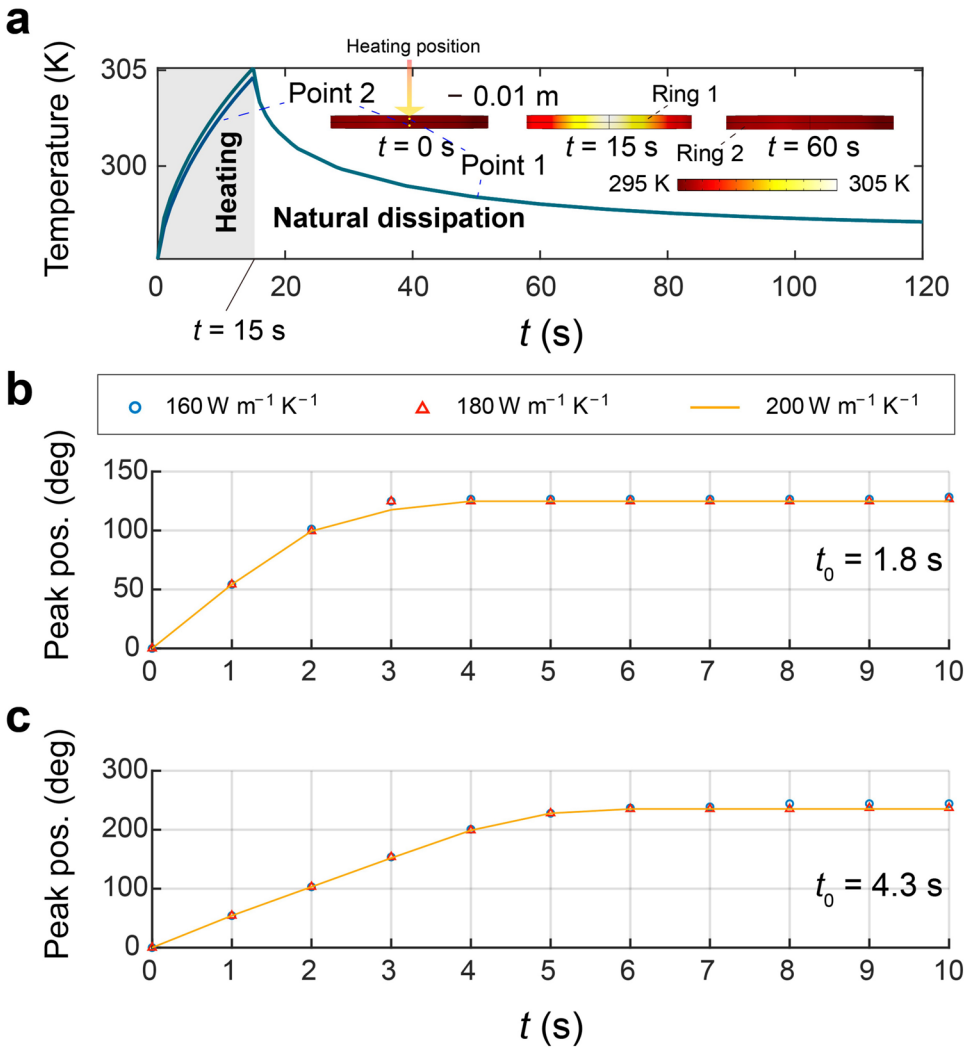

Extended Data Fig. 5 | Quantifying the impact of residual contact thermal resistance. a, Finite-element simulation of the experimental stack with identical geometry and parameters but zero interfacial resistance (heating on Ring 1 with power of $q(\theta) = -230\cos(8\theta - \pi)$ W, where $-\pi/16 \le \theta \le \pi/16$, for 15 s, then natural dissipation). Temperatures at two representative locations on the upper and lower layers (Points 1 and 2) become isothermal essentially immediately after heating is switched off, whereas the experiment with thermal grease shows cross-layer equilibration only after ~20 s (see Fig. S22). Insets: tangential temperature profiles at $t = 0$, 15, and 60 s (295-305 K), illustrating relaxation. Because both our initialization and waiting windows exceed 20 s, the residual resistance in the experiment does not affect the protocol timing. **b**-**c**, Robustness of temporal APT to interlayer transport variations: varying the effective thermal conductivity of the middle layer by ~ ±10% (κ = 160, 180, 200 W m^{-1}K^{-1}) leaves the propagation trajectory and trapping unchanged, as seen from the overlapping peak-position evolution for 1/3-cycle capture (**b**; t_0 = 1.8 s) and 2/3-cycle capture (**c**; t_0 = 4.3 s).

https://doi.org/10.1038/s41567-025-03129-8

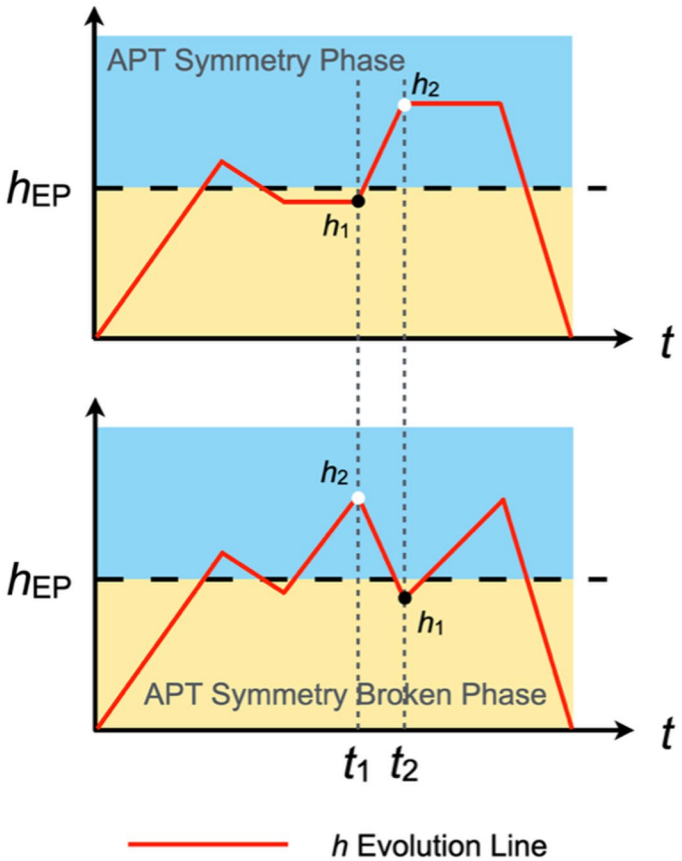

Extended Data Fig. 6 | The phase diagram controlled by the way of crossing the EP. The dashed line and the solid line denote the position of the EP and system's evolution trajectory, respectively. Black and white dots indicate two distinct coupling coefficients, respectively. In the upper panel, the phase diagram depicts the scenario in which the system evolves along their original temporal sequence. In contrast, the lower panel illustrates the phase diagram resulting from swapping the temporal order of the two coupling coefficients.

https://doi.org/10.1038/s41567-025-03129-8

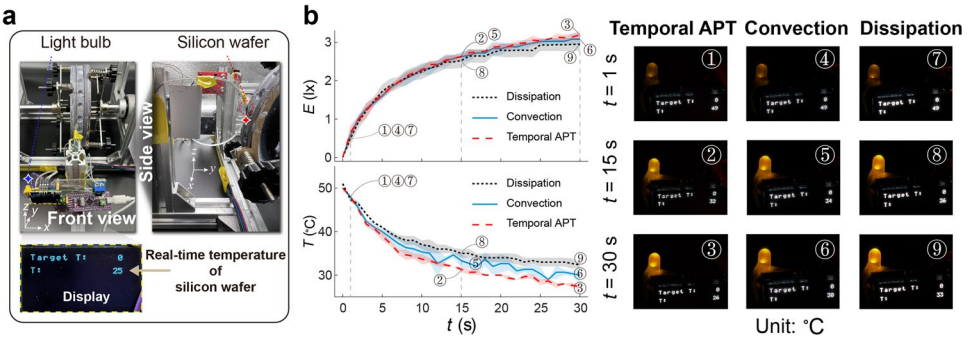

Extended Data Fig. 7 | Experimental demonstration of the heat trapping applied for cooling a silicon wafer. a, Experimental setup. The wafer is positioned in thermal contact at the 1/3 circumferential location of the ring—precisely where thermal energy is trapped by the heat trapping. The locally trapped cooling energy is obtained from the wafer, enabling active cooling. Additionally, the silicon wafer acts as a temperature-sensitive resistive component in an electrical circuit. As the wafer temperature decreases, its electrical resistance changes, thus modulating the current and adjusting the brightness of connected light bulbs. **b**, The left panels illustrate the temporal evolution of the silicon wafer's temperature (bottom panel, T in °C) and the corresponding illuminance (top panel, E in lx) of a light bulb, whose brightness is modulated by the wafer's temperature-dependent resistance. These profiles compare the cooling performance of the temporal APT (dashed curves), convection (solid curves), and natural dissipation (dotted curves). The right panels provide photographic snapshots of the light bulb's brightness and the simultaneously measured wafer temperature (displayed on the monitor, unit: °C) at selected time intervals: $t = 1$ s (images ①, ④, ⑦), $t = 15$ s (images ②, ⑤, ⑧), and $t = 30$ s (images ③, ⑥, ⑨) for the trapping, convection, and dissipation methods, respectively. Error bars (shaded regions) indicate one standard deviation based on three independent measurements.

https://doi.org/10.1038/s41567-025-03129-8

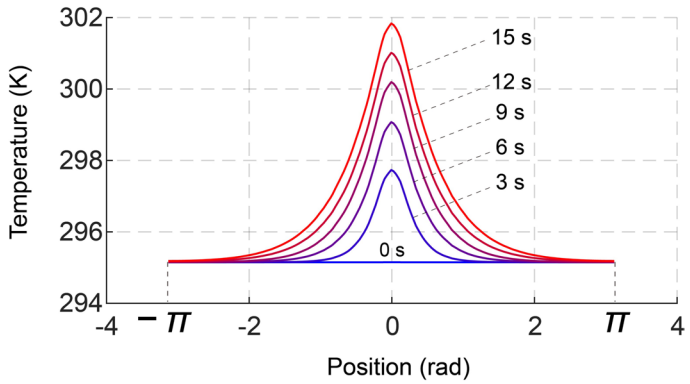

Extended Data Fig. 8 | Evolution from a localized hot spot to a first-harmonic ($\cos\theta$) profile on Ring 1. Finite-element simulation replicating the experimental hot-air initialization: a tangentially localized boundary heat flux $q(\theta) = -230 \cdot \cos(8\theta - \pi)$ W, where $-\pi/16 \le \theta \le \pi/16$, is applied for 15 s. Curves show the tangential temperature profile $T(\theta, t)$ at $t = 0, 3, 6, 9, 12$, and 15 s. Fast advection and diffusion broaden the initially localized heating into a first-harmonic-dominated waveform, approaching a cosine-like envelope by ~10-15 s. This validates the use of a $\cos\theta$ initial condition in simulations and is consistent with the demonstrated robustness to waveform in Supplementary Section 11. Position is plotted as θ (rad) over $[-\pi, \pi]$.

https://doi.org/10.1038/s41567-025-03129-8

Extended Data Table 1 | Room temperature for each panel in Fig. 4

Room Temperature	1 st. Test	2 nd. Test	3 rd. Test
Fig. 4b	24.6 °C	24.8 °C	24.9 °C
Fig. 4c	25.8 °C	24.8 °C	24.4 °C
Fig. 4d	24.3 °C	24.2 °C	24.4 °C
Fig. 4e	23.4 °C	23.1 °C	23.1 °C